Automated segmentation of tissue images for computerized IHC analysis

S. Di Cataldo*, E. Ficarra, A. Acquaviva, E. Macii

Department of Control and Computer Engineering, Politecnico di Torino, Corso Duca Degli Abruzzi 24, 10129 Torino, Italy

ARTICLE INFO

ABSTRACT

This paper presents two automated methods for the segmentation of immunohistochemical tissue images that overcome the limitations of the manual approach as well as of the existing computerized techniques. The first independent method, based on unsupervised color clustering, recognizes automatically the target cancerous areas in the specimen and disregards the stroma; the second method, based on colors separation and morphological processing, exploits automated segmentation of the nuclear membranes of the cancerous cells. Extensive experimental results on real tissue images demonstrate the accuracy of our techniques compared to manual segmentations; additional experiments show that our techniques are more effective in immunohistochemical images than popular approaches based on supervised learning or active contours. The proposed procedure can be exploited for any applications that require tissues and cells exploration and to perform reliable and standardized measures of the activity of specific proteins involved in multi-factorial genetic pathologies.

© 2010 Elsevier Ireland Ltd. All rights reserved.

1. Introduction

In this paper we address the problem of immunohistochemical tissue image segmentation.

In the last few years biological imaging has definitely undergone a revolution and new techniques have been shown to be effective in extracting clinical and functional information from images of molecules and tissues. In particular, the quantification of the activity of specific proteins through the analysis of tissue images provides critical information about important multi-factorial genetic pathologies, such as cancer. For example, EGFR/erb-B family of receptors plays an important role for non-small cell lung carcinoma (NSCLC) development. Quantifying and classifying the EGFR expression and activity in NSCLC with special regard to the assessment of the prevalence of EGFR mutations as well as

to ligand–receptor interactions lead to new insights into the modulation of EGFR in individual lung carcinomas [1].

In addition to its well-established role in the early diagnosis of cancerous diseases, protein expression analysis recently acquired a new important role in the design of novel targeted therapies: the correlation of standardized measurements of protein expression from pathological tissue images with genetic expression data extracted from the same tissues allows to define a group of potential candidates to protein family-inhibiting therapies as well as to classify the specific pathology in a more accurate way through its specific genetic alterations [1–3].

A widespread technique in this field which leads to protein activity quantification is immunohistochemistry (IHC), that is the analysis of cancer tissue images where marked antibodies are used to link specific proteins in situ, as well as their

---

* *Corresponding author.* Tel.: +39 11 564 7072; fax: +39 11 564 7099.
  E-mail addresses: santa.dicataldo@polito.it (S. Di Cataldo), elisa.ficarra@polito.it (E. Ficarra), andrea.acquaviva@polito.it (A. Acquaviva), enrico.macii@polito.it (E. Macii).

ligands; the evaluation of the colored stains at the specific subcellular regions where the markers are localized (i.e. nucleus, cellular membrane, cytoplasm) provides important information for the assessment of cancer [1]. Fig. 1 shows three images taken from different tissue specimens, where brown and blue stained regions indicate that the relative marker is present.

In the last few years this technique has acquired a central role in pathology thanks to its several advantages over alternative bioimaging techniques (e.g. fluorescence in situ hybridization, FISH); among them, its wide availability, low cost, easy and long preservation of the stained slides [4].

Currently, pathologists usually resort to slow, manual analysis to extract information from IHC images. This is time-consuming, not scalable for very large datasets and extremely affected by inter- as well as intra-operator variability [5]. Moreover, IHC's new role in target therapy response prediction and in the correlation of protein and genetic expression data [1–3] is placing new demands on the reproducibility of the obtained information [6]. This calls for new automated tools able to assist the pathologist in their examinations and to provide fast, accurate and standardized measures of protein activity in IHC images.

Protein expression has to be computed within the specific subcellular location of interest of the analyzed receptors (nuclei, cellular membranes or cytoplasm, depending on the receptor) in order to obtain sensible biological information [1]; in fact the subcellular location in which the receptors are expressed may represent a very small percentage of the whole imaged area. This translates into a cell-by-cell evaluation of the subcellular stain, that is much more specific than simple quantification of the global amount of the stain in the whole image [7,8] and that requires preventive recognition of the cancer cells in the specimen and accurate segmentation of the subcellular compartments where the target receptors are localized.

In this paper we present fully automated techniques that exploit: (i) recognition of the cancerous cells and separation from the non-cancerous tissue areas in the specimen (e.g. stroma) and (ii) segmentation of cancerous nuclei in the areas identified at point (i). The proposed procedure can be exploited to perform reliable and standardized measures of protein activity as well as for any other applications that require tissue and cell exploration.

To this day, literature does not provide effective fully automated procedures to perform the tasks addressed by this paper. Commercial microscopy software usually allow the user to select the subcellular location of interest for protein activity quantification in a semiautomated or automated way; nevertheless, these tools are based on simple approaches that suffer due overgeneralization, and most of the times require extensive user interaction, so that the objectivity of the result tends to be lost [4,6,9,10]. In particular, commercial products generally require the user to select manually the areas that are richest in tumoral cells [11,12], to set intensity thresholds or levels to distinguish the cellular patterns from the background [13,14] or to outline a set of cells that are representative of the tumor or of the specific targeted cellular regions [15,16]. Moreover, most of these commercial tools are integrated into whole-slide scanning instruments [11,16] or are hardware-based in that they require multispectral imaging technologies attached to microscope platforms that may be not readily available to a regular pathologist or onchologist [15,17].

The recent literature reports many attempts to develop automated methods for nuclear segmentation. The used approaches vary among the most widely known image processing techniques, including intensity thresholding [18,19], active contours [20–24], watersheds [24–26], multiscale analysis [27], a priori geometric models [28,29], graph-cuts [30], Markov random fields [31], etc. Despite active research in this field, reliable cancerous nuclei segmentation remains extremely challenging.

The major contribution of this paper is to provide a fully automated and flexible procedure that overcomes the limitations of the existing computer-based techniques.

The paper is structured as follows: in Section 2 we discuss the main challenges related to IHC tissue image segmentation and limitations of the existing techniques and we describe the main contributions of our work; in Section 3 we present our case study related to the IHC analysis of lung cancer tissue images and we describe in detail our proposed methods; in Section 4 we discuss parameters and implementation; in Section 5 we present experimental results; in Section 6 we conclude the paper.

2. Background

2.1. IHC analysis and image characteristics

The images targeted by our methods are high-resolution microscopy pictures of tissue samples stained with marked antibodies [1] (see Fig. 1 for examples).
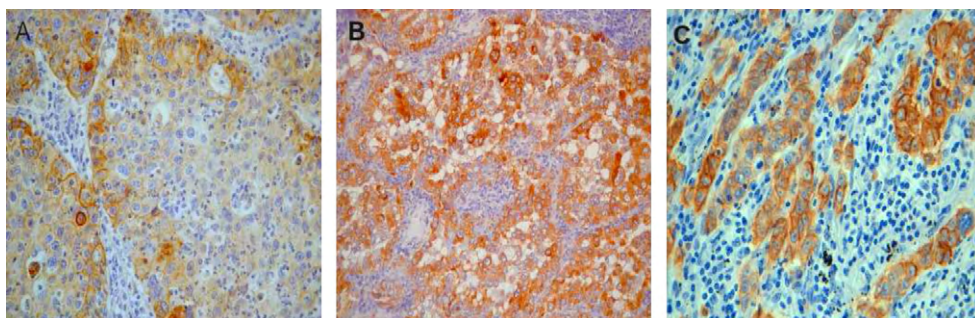
Fig. 1 – Examples of IHC lung cancer tissue images. (A) 400× image with membrane activity; (B) 200× image with cytoplasm activity; (C) 800× image with membrane activity.

In general, IHC techniques use different stains to detect the activations of specific proteins and distinguish them from regions without activations. The purpose of IHC image analysis is to separate the activated image regions from the rest of the image. Literature reports several methods and protocols for the quantification of IHC specimens [32], which generally include both evaluation of the intensity and of the continuity of the staining in the specific subcellular location that is targeted by the receptors. In particular, this analysis requires: (i) identification of the cancerous areas in the tissue sample, (ii) cell-by-cell identification of the subcellular compartments of the cancerous cells (i.e. nuclei, cellular membranes or cytoplasm) that are targeted by the given receptors, and then (iii) at the only locations of interest previously identified, cell-by-cell evaluation of the staining and of the percentage pixels that are positive to the target receptors. The positive portions are highlighted by a more intense coloration compared to the negative ones, that are just lightly stained or not stained at all. These cell-by-cell measures will be then categorized into three or four groups (typically 0 to 3+) in order to obtain a scoring of protein expression in the whole sample [28,33].

In this paper we focus on the first two steps of the procedure. In particular we discuss the segmentation of nuclear membranes, that is a critical task not only for the quantification of images with nuclear activity [18] (i.e. where receptors activations are specifically localized in the nuclei), but also for images with cellular membrane and cytoplasm activity (see Fig. 1): in fact nuclear membranes are generally used as reference curves to detect cellular membranes and cytoplasm [28,33].

The main features of IHC images that make the selection of the cancerous tissue and the segmentation of nuclear membranes challenging are:

1. the presence of tissue components that are not of interest for the analysis (i.e. lymphoids, blood vessels, noncancerous tissue components, etc.);
2. the superposition of different tissue slices, due to the unidealities of the sample preparation process [6];
3. the colocalization of different stains [8];
4. the presence of clustered or touching cells;
5. the non-predictable morphological variations of the tissue induced by the pathological process;
6. the heterogeneity (in terms of both intensity gradient and color) of the regions to be recognized. This is mainly due to:
   (a) the uneven activation intensity leading to variable color intensity;
   (b) the superposition of different colors due to the unideal distribution of the stains on the reactive regions and the superposition of different tissue layers;
   (c) the variation of the illumination over the tissue specimen.

These heterogeneities are intrinsic of IHC technique, which is renowned for being affected by many sources of variability related to the preparation of the samples as well as to the acquisition of the images (e.g. fixation conditions, specimen pretreatment, reagents and detection methods) [6].

2.2. Related works and contributions

The image characteristics described in the previous section make IHC tissue segmentation a challenging task. In the last few years there have been many efforts towards the development of automated methods for nuclear segmentation; nonetheless, to these days literature does not provide any fully automated procedure able to cope with all the critical issues discussed in Section 2.1.

Stains' colocalization, which is a frequent phenomenon in IHC imaging, is a highly critical issue for most of the methods based on classical color segmentation [7,8]. Several methods in literature classify pixels on the base of their red–green–blue (RGB) values [29,34] or of color features obtained by transforming the RGB image information to hue-saturation-intensity (HSI), hue-saturation-value (HSV), CIELab [8,28] or other color specific representation such as blue/red ratio and green channel [35]. Nevertheless, most of the color segmentation techniques present problems in presence of stains' colocalization [8], since pixels are classified as belonging to a stain or to another one but more than one dye may have contributed to the final color. Color classification methods do not necessarily exclude stains' colocalization, since mixed colors can be classified on the base of their proximity to the features that are representative of one of the pure color classes. Some methods even overcome the problem of class non-separability due to color mixing by using masks that modify the ambiguous pixel values [34], although these solutions provide reliable distinction between positive and negative cells rather than stain-specific intensity information.

The inhomogeneous staining and illumination of the specimen complicates the distinction between foreground and background and leads traditional intensity-based segmentation techniques such as global intensity thresholding [18,19] to error.

The effectiveness of other widely used segmentation methods such as edge-based techniques (e.g. Canny [36]), active contours [20–24] or watersheds [24–26] is limited by the remarkable intensity variations within as well as outwards the targeted cellular regions. In particular, active contours are highly impacted by the hard noise conditions, the non-predictable intensity variations within the nuclei and the massive presence of close or overlapped foreign particles which may deviate the initial curve from the target boundary. In Section 5 we report results obtained applying active contours to the segmentation of nuclear membranes. Watersheds approaches [24,25] are rather affected by oversegmentation and multiple watershed lines; the attempt to overcome over-segmentation through seeded watersheds [26] presents problems in obtaining only one seed per object and often resorts to extensive user-interaction. In our approach watersheds are used just to separate clustered nuclei; then correction steps based on morphology and gradient magnitude analysis are applied to overcome over-segmentation. Edge-based techniques include also multiscale analysis [27], that can handle intensity variations but do not address overlapping nuclei with weak edge information.

Techniques based on geometrical templates or on fixed models of the tissue morphology [28,29] suffer due overgeneralization because of the non-predictable shape and size

variations of the cells; these variations are induced by the pathology as well as by the mechanical and thermal stress related to the preparation of the sample.

Alternative approaches include graph-cuts methods [30], that depend on manual initialization, and Markov random fields [31], that suffer due undersegmentation.

The several sources of variability that naturally affect IHC imaging [6] reflect in the heterogeneity of the features of the produced images, so that supervised learning techniques based on mathematically superior methods such as support vector machines [37] (SVMs) suffer from classes' non-separability due to the heterogeneity of the training sets. In Section 5 we report experimental results obtained applying SVMs to the selection of the cancerous tissue.

In conclusion, most of the times manual intervention is still necessary to resolve difficult/ambiguous cases. Recent literature reports examples of automated techniques for cell and nuclear segmentation of microscopy images; nevertheless, most of these techniques are specifically intended to fluorescent cellular images [24,38], where each dye is identified by a specific emission wavelength, so that the cellular structures of interest (such as nuclei) can be easily isolated from the rest of the tissue and visualized in a specific channel. Other techniques exploit nuclear segmentation of IHC images with nuclear activations [18,39], that are less noisy and relatively easier to segment than images with membrane or cytoplasm activations.

Our proposed method is mainly a color and morphology-based procedure; as such the novelty of the method is in how color segmentation and morphological operators are applied in the specific context of IHC tissue imaging in order to solve the technical problems that are typical of this field. Summarizing, the main contributions of our paper are the following: (i) we exploit morphological and chromatic characteristics of the tissue in order to recognize the cancerous tissue automatically, thus avoiding the necessity of manual selection of the target tissue areas; (ii) we separate nuclei from background by exploiting local analysis of intensity distribution in the neighborhood of each cell; this leads to minimize the effect of noise as well as of uneven staining and illumination, that are major problems in IHC imaging; (iii) we separate clusters through watershed algorithm and then we correct watersheds oversegmentations through an innovative technique which merges oversplit nuclei by exploiting chromatic characteristics of the cells.

3. Materials and methods

3.1. *Case study: segmentation of lung cancer IHC tissue images*

In this paper we applied our proposed techniques to images of lung cancer tissue (see Fig. 1 for examples). This is an application of great importance in biomedicine: in fact lung cancer is one of the leading causes of death for tumor: despite extensive preclinical and clinical research has been led for decades, lung cancer's prognosis is still very low with only 5–15% of patients surviving 5 years after the first diagnosis. The characteristics of these images entail all the challenges mentioned

in the previous sections and for this reason they represent a meaningful case study for our approach. However, the robustness of our algorithm was assessed also in tumors from other anatomical locations (e.g. kidney, liver, prostate and bone marrow).

Images were acquired from surgical samples of anonymous patients fixed in formalin and embedded in paraffin. From each paraffin block, 5-μm-thick sections were prepared. After deparaffinization and rehydration through graded alcohols and phosphate-buffered saline (pH 7.5), endogenous peroxidase activity was blocked by absolute methanol and 0.3% hydrogen peroxide for 15 min. The slides were incubated for 40 min at room temperature with primary monoclonal anti-EGFR antibody (dilution, 1:60; NeoMarkers, Freemont, CA) or with primary monoclonal anti-TGF-alpha antibody (dilution, 1:300; Calbiochem, Merck, Darmstad, Denmark). The immune reaction was revealed in a biotin-free detection system based on a dextran chain linked to the secondary antibody and carrying peroxidase (En Vision; Dako, Glostrup, Denmark), using 3,3-diaminobenzidine (DAB) as the chromogen. For antigen retrieval steps, the sections were treated in a microwave oven for 15 min in EDTA buffer (pH 8.0). Slides were counterstained with hematoxylin (H), dehydrated, and mounted.

The images to be processed are then characterized by brown (DAB) and blue (H) stains; the relationship between stains and tissue parts are resumed in Fig. 2.

A brown DAB stain highlights the specific portion of the cancerous tissue that shows positive reactions at the EGF-R/erb-B or at the TGF-alpha receptor activation. These positive reactions are localized in the cellular membranes or in the cytoplasm of the cancerous cells, respectively for EGF-R/erb-B and TGF-alpha (see Fig. 2A), so that images with EGF-R/erb-B reactions are called images with membrane activity, whereas images with TGF-alpha reactions are called images with cytoplasm activity.

A blue hematoxylin stain is used as a contrasting background color; it highlights:

1. the cancerous portions that are negative to the target receptors (i.e. nuclei as well as parts of cellular membranes or of the cytoplasm that do not react to the studied receptor) (see Fig. 2B and C);
2. the non-cancerous portions (lymphoids, blood vessels, stroma, etc.) present in the sample because of unidealities in the selection of the tissue (see Fig. 2D).

In particular, nuclei of both cancerous and non-cancerous cells are always blue-colored, with the H stain revealing their chromatin content; the blue coloring of the chromatin is generally more intense, so that nuclei are distinguishable from the background tissue (see Fig. 2B).

3.2. *Proposed procedure*

Our procedure is based on three consequential step:

1. **Colors separation**, in which a pure hematoxylin (blue) and a pure DAB (brown) image are obtained from the original RGB picture.
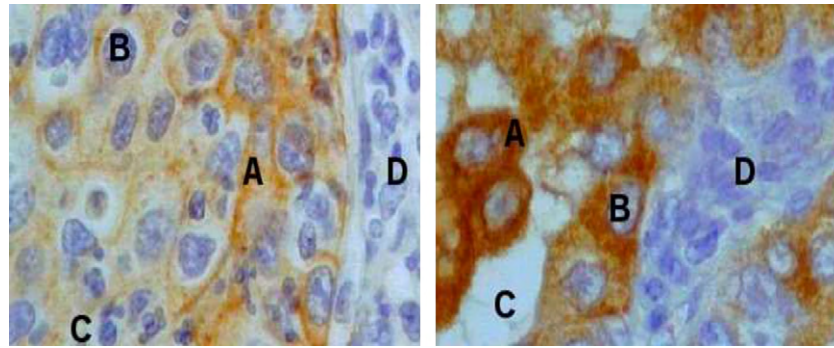
Fig. 2 – Details of IHC lung cancer tissue images with membrane (left) and cytoplasm activity (right). (A) Positive reactions at the targeted receptors; (B) cancerous nuclei; (C) negative reactions at the target receptors; (D) non-cancerous tissue (stroma, lymphoids, blood vessels, etc.).

2. **Selection of cancerous tissue**, in which the cancerous tissue is automatically separated from the non-cancerous components (e.g. stroma).
3. **Segmentation of nuclei**, in which the nuclear membranes of the cancerous cells highlighted by step 2 are detected and outlined.

For step 1 we applied a specific literature approach, whereas for selection of cancer tissue and nuclei segmentation we developed custom-designed procedures. All the phases of the algorithm are detailed in the following subsections and reported in the flowchart of Fig. 3, whereas the set-up of parameters is reported in Section 4.

3.2.1. Colors separation

The purpose of this first method is the separation of the brown (pure-DAB) and blue (pure-hematoxylin) components of the RGB image; in this way the specific information carried by the two stains, which highlight different cellular structures in the tissue, can be processed separately. The main challenge of this task is to obtain an effective color separation in presence of stains colocalization, a very common phenomenon in IHC tissue images due to the chemical reactions of stains linking the target proteins and to the tissue superposition during the slicing of the samples. A powerful approach to achieve this target is color deconvolution [40]. It is a method based on the stain-specific RGB absorption which has been demonstrated to separate reasonably well up to three overlapped stains in presence of stains colocalization [8]. The technique can be applied not only to H-DAB images but to any of the most used dies in histopathology (e.g. H-E, H AEC Azan-Mallory, Fast Red, and Fast Blue and DAB) or to any user-defined die, provided that its RGB components are experimentally determined and given as an input to the algorithm. The information carried by the pure-brown and the pure-blue images as obtained after color separation are processed to perform cancer tissue selection and nuclear membranes segmentation.

In order to get the best performance achievable from color deconvolution, we followed the indications provided by Ruifrok and Johnston [40] and Landini [41]. As for most colors segmentation techniques, color deconvolution may not produce meaningful results in case of nuclear stains with mixed high-intensity hematoxylin and DAB staining [7]. This problem does not arise in images with cytoplasm and membrane staining. In order to obtain reliable nuclear segmentations in case of nuclear staining, the separate contributions of H and DAB stains have to be merged together (see end of Section 3.2.3).
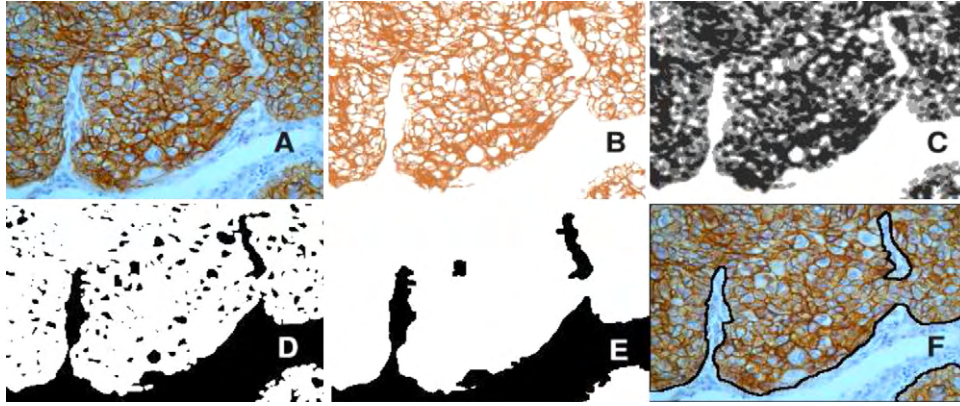
3.2.2. Selection of cancerous tissue

This method addresses the automated recognition of cancerous tissue from non-cancerous areas (e.g. sroma, blood vessels), thus avoiding the necessity of time-consuming and not feasible manual selection.

Our method exploits both color and morphological information to distinguish cancerous and non-cancerous areas. First of all we apply unsupervised clustering to partition the sample into regions that are homogeneous in terms of brown stain intensity, exploiting region-wise rather than pixel-wise color information in order to deal with color inhomogeneity that is typical of IHC images. Then we apply morphological processing in order to obtain the final tissue classification, thus associating the tissue regions as obtained from the previous step to *cancerous* or *non-cancerous tissue*.
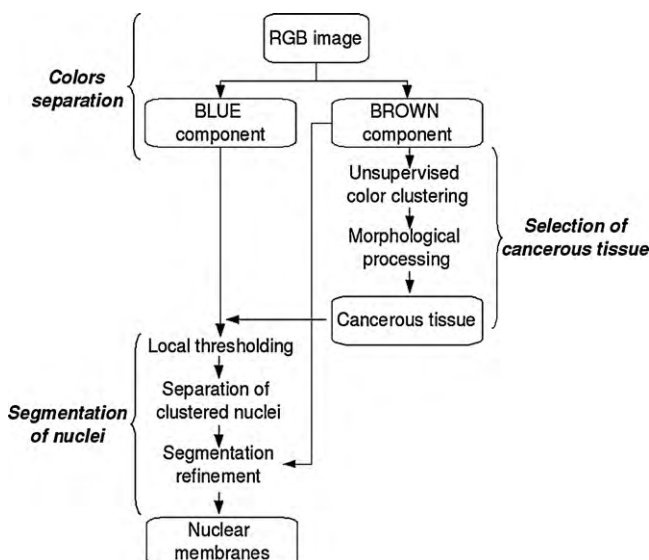
Fig. 3 – Flowchart of the proposed technique.

Fig. 4 – Selection of cancer tissue. (A) Original image; (B) pure-brown image, where the cancerous tissue is locally brown colored while non-cancerous tissue appears while or very light brown; (C) gray-level representation of the discriminant feature F used for color clustering, where the non-cancerous tissue is characterized by the highest value of F (white); (D) highest centroid value obtained after k-means clustering, containing both non-cancerous tissue and small round-shaped portions of negative cancerous cells; (E) final tissue segmentation after morphological processing (cancerous tissue in white, non-cancerous tissue in black); (F) manual tissue segmentation, shown for comparison. (For interpretation of the references to color in this figure legend, the reader is referred to the web version of the article.)

Given the characteristics of the IHC images, an unsupervised approach was found to be better than approaches based on supervised learning, such as support vector machines [37,42]; in fact our experimental results show that SVMs are not able to deal with the heterogeneity of the training features (see Section 5 for further details).

The main steps of our procedure are detailed in the following subsections and shown in Fig. 4.

3.2.2.1. Unsupervised color clustering. A preliminary partition of the tissue sample is performed through unsupervised clustering of color information taken from pure-DAB image, as obtained from the colors separation step. This technique is based on the assumption that cancerous pixels are either brown colored or rather have some brown colored regions in their vicinity; in fact the brown stain highlights only the portions of the cancerous tissue (i.e. cellular membranes or cytoplasm, respectively) that are positive to the target receptors. Then in our technique each pixel is assigned to a different cluster depending on the brown intensity which is characteristic of its surrounding area, and not just of the pixel itself. In particular, the discriminant feature we used is the following:

$$F(x, y) = \text{Min}_N \langle \bar{I}_N \rangle, \tag{1}$$

where x and y are the pixel's coordinates, N is a neighborhood of radius R_N and $\bar{I}_N$ is obtained by the pure-brown image I by averaging the intensities over each pixels' neighborhood N. Then the discriminant feature $F(x, y)$ related to the pixel with coordinates x and y is calculated as the minimum value of all the average intensities in its neighborhood N; this corresponds to the mean intensity value of the darkest brown area around the pixel. Pixels that do not have any positive region in their vicinity are characterized by high values of $F(x, y)$ whereas pixels that have positive regions in their vicinity are characterized by low values of $F(x, y)$; in fact light brown areas correspond to high intensity values, and so to high values of F, and vice versa.

The radius of the neighborhood R_N is dependent on the cell size, and thus on image resolution (see Section 4 for details).

Cancerous tissue is generally characterized by more than a value of $F(x, y)$: in fact the brown stain is generally lighter or darker in different portions of the cancerous tissue, depending on how positive to the target protein activation that portion is. Generally pathologists classify the staining into three or four classes [32]; to be consistent with this praxis, we partitioned the pixels into four clusters. This choice was corroborated as well by our experiments on real IHC images.

The clusters' partition was exploited through a well-established iterative unsupervised learning algorithm, namely k-means [43]. The cluster that is characterized by the highest centroid value, i.e. by the highest mean value of F, is constituted by tissue areas that are negative to the target receptor; as shown by Fig. 4D, this cluster include non-cancerous regions as well as small round-shaped cancerous regions without receptor activation (such as nuclei and negative cancerous cells); the other three clusters are constituted by only cancerous tissue areas, that are positive to the target receptor.

3.2.2.2. Morphological processing. In order to obtain the final separation of cancerous and non-cancerous tissue, pixels belonging to cancerous portions that are negative to target receptor have to be selectively removed from the highest centroid cluster as obtained from the previous described K-means clustering. This is achieved through morphological processing. In particular, we perform a selective removal of particles with low area and high circularity; in fact, as shown by Fig. 4D, negative cancerous portions are small and round-shaped. Area was measured in terms of number of pixels belonging to each particle, circularity was measured trough the following index in the [0,1] interval:

$$\text{circularity} = 4\pi \frac{\text{area}}{\text{perimeter}^2} \tag{2}$$
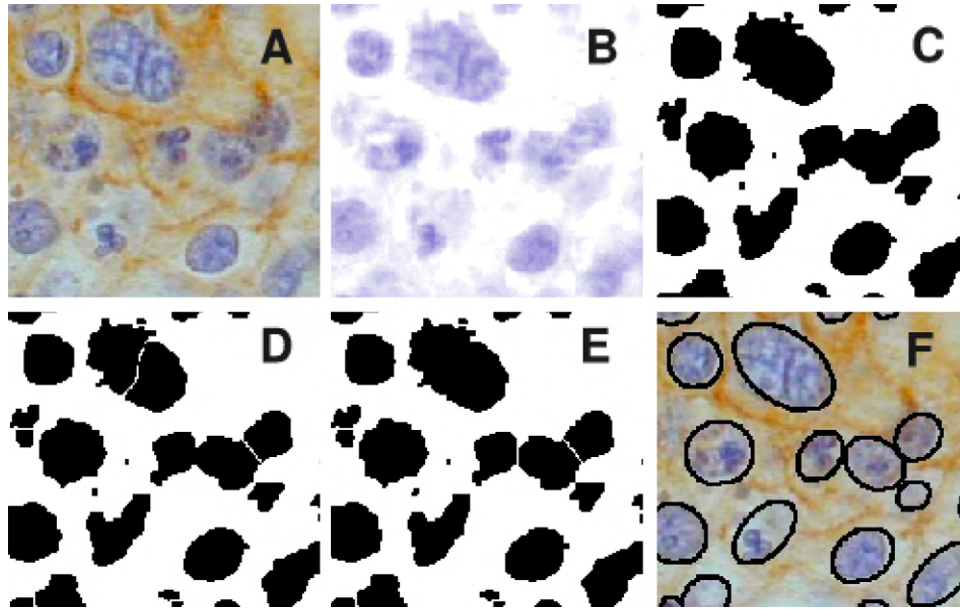
Fig. 5 – Segmentation of nuclei. (A) Original image; (B) pure-blue image; (C) after local thresholding; (D) after separation of clustered nuclei through watershed algorithm; (E) after remerging oversplit nuclei; (F) final segmentation. (For interpretation of the references to color in this figure legend, the reader is referred to the web version of the article.)

Threshold values of area and circularity, T_A and T_C, respectively, are reported in Section 4.

Secondly, non-cancerous tissue usually shows a well-defined boundary w.r.t. cancerous background in terms of intensity gradient variation (see Fig. 4B), so that other cancerous regions can be removed from the highest centroid cluster through their edge characteristics. Therefore areas which show along their boundary a low percentage of edge pixels, i.e. pixels with high gradient intensity variation w.r.t. background, are selectively removed from the cluster (threshold value T_E is reported in Section 4). Edge detection is performed through a Sobel detector followed by automated intensity thresholding [44].

As shown in Fig. 4E, the highest centroid cluster as obtained after supervised color clustering and morphological processing contains non-cancerous tissue; the complementary region represents the cancerous tissue.

3.2.3. Segmentation of nuclei

The third method in our framework is the segmentation of cancerous nuclear membranes.

Our proposed technique is a structured procedure that exploits color and morphological information. Pipelined steps of this procedure, that are necessary to cope with the aforementioned critical issues of IHC tissue images, are described in the next subsections and shown in Fig. 5.

3.2.3.1. Local thresholding. Since nuclei are revealed by the blue stain, our technique for nuclear segmentation exploits color information taken from the pure-blue image as obtained from the colors separation method. Since in the pure-blue image nuclei are characterized by darker coloring (i.e. lower intensity values) compared to background, they are detected through automated intensity thresholding (see Fig. 5C).

To overcome variations of staining and illumination we apply a local adaptive threshold dependent on the local intensity distribution. The procedure is customized by calculating thresholds based on the analysis of local intensity distribution of each pixel, which aims at minimizing the effects of unrepresentative pixel values due to noise and stain inhomogeneity by preventively subtracting each pixel's intensity by the median value of its neighborhood. The neighborhood size, namely local thresholding radius R_{LT}, is selected taking into account the average dimension of the nuclei; thus its value is mainly dependent on image resolution (see Section 4 for details).

Binary morphological operations [44] (dilation, closing and holes filling) are applied after thresholding to handle intensity variations within the nuclei and irregular nuclear shapes.

3.2.3.2. Separation of clustered nuclei. Clustered nuclei are separated through watershed algorithm [44]. In our method we get rid of the well-known over-segmentation problems of watershed technique through a selective remerging of oversplit nuclei (see Fig. 5E). This is obtained by scanning the interposed area between each couple of nuclei split by watershed and by computing the relative amount of blue and brown pixels within this area. Blue and brown are obtained respectively from the pure-brown and the pure-blue image though local intensity thresholding. Couples of particles with a prevalence of brown pixels (that belong to cellular membrane or cytoplasm) in the interposed area are interpreted as two separated nuclei and left unchanged; to the contrary couples of particles with a prevalence of blue pixels (that belong to nuclei) in the interposed area are interpreted as a single nucleus and remerged. This is obtained by comparing the percentage of blue and brown pixels in the interposed area between the two particles to threshold per-

Table 1 – Parameters set for cancer tissue selection (upper part) and nuclear segmentation procedures (lower part).

	Parameter	Value	Section
$R_N\star$	Neighborhood radius	5px (200×), 10px (400×), 20px (800×)	3.2.2.1
k	Number of k-means clusters	4	3.2.2.1
$T_A\star$	Area threshold	1000px^2 (200×), 2000px^2 (400×), 4000px^2 (800×)	3.2.2.2
$T_C\star$	Circularity threshold	0.7	3.2.2.2
T_E	Edge threshold	25%	3.2.2.2
$R_{LT}\star$	Local thresholding radius	21px (200×), 42px (400×), 84px (800×)	3.2.3.1
T_{blue}, T_{brown}	Percentages of blue and brown pixels between two nuclei	40%, 50%	3.2.3.2
$T_S\star$	Threshold for size selection	40%	3.2.3.3

Parameters' values were tuned on lung cancer tissue images. Parameters that are related to the morphological characteristics of the tissue are highlighted by $\star$. Values are provided for three different image enlargements (200×, 400×, 800×).

centage values, namely T_{blue} and T_{brown} (see Section 4 for details).

3.2.3.3. *Segmentation refinement.* One of the major challenges of cancerous nuclear segmentation is the presence in the sample of other particles (e.g. non-cancerous nuclei and lymphocytes) together with the target nuclei; these foreign particles may be very similar to the target nuclei in terms of shape and color, thus leading nuclear segmentation to error. The presence of non-cancerous tissue in the sample is already overcome in our procedure by the automated tissue selection step, which allows to preventively narrow the range of interest of nuclear segmentation to the areas of the image that are occupied by the cancerous tissue. Nonetheless lymphocytes, which are round-shaped and blue-colored exactly as the cancerous nuclei, may be spread all over the sample, thus calling for specific postprocessing to remove them from the segmented nuclei. Lymphocytes' removal is performed based on their smaller size comparing to cancerous nuclei: in particular, particles whose area is considerably lower than the average area of all the detected nuclei are removed from the final segmentation. The threshold size T_S is expressed in terms of percentage of area w.r.t. the average area of the detected nuclei and reported in Section 4.

In order to obtain smooth nuclear membranes, the best fitting ellipse is finally calculated and outlined for each detected nucleus (see Fig. 5F).

The proposed procedure can be opportunely simplified in order to address images with nuclear staining. In fact in images with nuclear staining both the dyes highlight the nuclei, that are clearly distinguishable from background and then generally easier to segment. Then nuclear segmentation in this case can be obtained by simply applying the local thresholding step on both pure-blue and pure-brown images separately and then by merging together the respective binary results. Separation of clusters can be obtained through classical watersheds.

4. Implementation

We implemented our procedure in Java as a plugin for ImageJ [45], a powerful public domain image analysis and processing software which runs on all standard operating systems (Windows, Mac OS, Mac OS X, Linux); therefore it is totally hardware-independent, flexible and upgradeable. We

inherited the whole class hierarchy of ImageJ 1.38 API and open-source plugins and macros in [41,46,47] and we implemented our own functions and classes.

Parameters' values tuned on real-life lung cancer tissue images are shown in Table 1 separately for the selection of cancer tissue and the segmentation of nuclei; they do not need to be changed for lung cancer tissue images with either membrane and cytoplasm activity as well as for weakly and strongly stained tissues. As clarified in the description of our techniques in Section 3, most of the parameters (highlighted with a $\star$) are related to morphological features of the tissue to be segmented, thus they were set taking into account the specific characteristics (cell size and shape) of the lung tissue; the user is anyhow allowed to apply the procedure to other tissues with different morphological characteristics by tuning these parameters. A user-friendly interface allows the setting of different parameters' values without modifying the source code. The other parameters' values are related to general characteristics of IHC images: in particular, the number of clusters k is consistent with the number of intensity levels usually discriminated by pathologists and the values of T_E, T_{blue} and T_{brown} are related to how the blue and the brown stains are distributed in a specimen while highlighting different tissue components. See Section 3 for explanation of each parameter.

5. Experimental results

We tested the performance of our automated pipeline on real IHC images of lung cancer tissue. H-DAB staining was preventively performed on the tissue to highlight positive activations at the EGF-R or TGF-alpha receptors, that are respectively localized in the cellular membrane or in the cytoplasm of epithelial cells (see Section 3.1 for details). Other than the cancerous epithelial cells, that are the ones targeted by IHC analysis, the tissue samples contained portions of non-cancerous connective stromal tissue as well as lymphocytes and other foreign particles. The images were acquired through high resolution digital microscopy with three different enlargements (200×, 400× and 800×).

Our proposed techniques for the selection of the target tissue and the segmentation of nuclei were firstly tested separately, since they represent conceptually independent tasks of the automated pipeline for tissue segmentation. The experiments as well as the achieved results are reported in

Sections 5.1 and 5.2, respectively for the selection of the target tissue and for nuclear segmentation. The two sections are both organized as follows. In a first subsection the performance of the automated technique is assessed through strict pixel-wise comparisons with manual segmentations provided by an expert of the field. In a second subsection it is compared with alternate techniques that are highly popular in data mining and computer vision, namely support vector machines (SVM) [37] and active contours [22]. The application of the above mentioned techniques to the tasks targeted by our work (respectively, SVM to the selection of the target tissue and active contours to nuclear segmentation) is discussed; the better accuracy provided by our approach is demonstrated through experimental results achieved on real IHC images. Finally, in Section 5.3 we reported the accuracy of the combined tissue selection + nuclear segmentation procedure, providing a measure of how the efficiency of the tissue selection technique impacted on the following segmentation of pathological nuclei.

5.1. Selection of cancerous tissue

5.1.1. Comparison with manual performance
In order to evaluate the performance of our technique in selecting the target tissue (i.e. in disregarding the unwanted non-cancerous areas), an expert of the domain was asked to outline manually cancerous and non-cancerous tissue in the validation datasets; then a pixel-wise comparison between automated and manual segmentations was performed. Validation datasets contained on average 1700×1300 pixels, for a total number of about 28 Mpixels, and were taken from real-life EGF-R and TGF-alpha tissue images.

The performance of the technique was evaluated in terms of sensitivity and specificity of removal of non-cancerous tissue. Sensitivity was calculated as percentage of non-cancerous pixels correctly identified; specificity was calculated as percentage of cancerous pixels correctly identified. The *accuracy* of cancer tissue selection was finally calculated as weighted[1] average of sensitivity and specificity, as follows:

$$\text{accuracy} = \frac{2}{3}\text{sensitivity} + \frac{1}{3}\text{specificity} \qquad (3)$$

The achieved results are reported in the first section of Table 2, under the label "unsupervised approach".

The accuracy on tissue segmentation was on average above 90%, thus confirming that tissue selections obtained through our automated unsupervised procedure are highly comparable with those manually performed by a skilled operator.

---

[1] A higher weight was assigned to sensitivity, since it is more critical than specificity for the automated quantification of protein activity, that is the principal application targeted by our pipeline. In fact to eliminate as much as possible non-representative tissue from the range of interest is fundamental for a reliable measure of protein activity. This is expressed by sensitivity of removal of the non cancerous tissue. Moderate removal of cancerous regions is rather tolerable, since it has a minor influence on the final result.

5.1.2. Comparison with supervised approach
Our unsupervised technique was compared with supervised learning approach. For this purpose we developed a specific procedure for the automated selection of the target tissue based on support vector machines [37], a theoretically superior machine learning method which has often been shown to achieve great classification performance compared to other learning algorithms across most applications and fields, including image processing and tissue segmentation [48].

In SVM method input elements (i.e. tissue regions, in this work) are classified as cancerous or non-cancerous on the base of a set of representative characteristics, the so called features vector. To perform a reliable classification, SVM is preventively trained with a set of pre-classified training instances. The classification is based on the implicit mapping of data to a higher dimensional space via a kernel function and on the consequent solving of an optimization problem which leads to identify the maximum-margin hyperplane that separates the given training instances; the hyperplane is calculated on the base of the boundary training instances (i.e. elements which are border-line between the two classes) rather than on the base of the entire training dataset: this leads SVM to a better efficiency w.r.t. other learning techniques (e.g. neural networks), especially with highly dimensional datasets. This is the reason why SVMs are getting more and more popularity among other supervised methods, especially for imaging applications. See [37] for more technical details about SVMs.

The SVM procedure we implemented for the selection of the target tissue in IHC images consists in three sequential steps:

1. **Generation of the training vectors**. Training vectors are generated by shifting horizontally and vertically a square window on a set of pre-classified images and by picking out RGB values of the pixels in the window; vectors with a prevalence of cancerous or non-cancerous pixels are labeled with a $+1$ or a -1, respectively.
2. **Training**. The labeled features vectors are fed into the SVM for the training.
3. **Classification**. The optimized SVM is used to perform tissue classification for new unclassified images.

See our previous work [42] for further details about implementation and parameters of the SVM technique.

In order to compare SVMs to our unsupervised approach we performed experiments on the dataset of real IHC tissue images described in Section 5.1.1. As for the unsupervised method, the accuracy of SVM technique was measured through pixel-wise comparison with ground truth consisting in manual segmentations provided by an expert of the field (see Eq. (3)); the manual segmentations were the same used to assess the accuracy of our method in Section 5.1.1. The results achieved by SVMs are reported in the second section of Table 2, under the label "supervised SVM approach".

Our method achieved the best results, overcoming the accuracy of SVM technique on average of 8.4%. Cancerous and non-cancerous tissues may show very variable characteristics in terms of morphology as well as color distribution; this is

Table 2 – Experimental results of unsupervised and SVM classifications.

Dataset	Unsupervised approach			Supervised SVM approach				
	Sensitivity (%)	Specificity (%)	Accuracy (%)	Number of training instances	Number of validation instances	Sensitivity (%)	Specificity (%)	Accuracy (%)
1 (200×)	88.49	91.58	89.52	1692	28,308	57.91	91.38	69.07
2 (200×)	89.08	83.02	87.06	912	20,263	94.05	79.20	89.10
3 (200×)	94.63	98.58	95.95	220	20,192	91.09	94.75	92.31
4 (200×)	87.58	87.04	87.40	408	19,142	84.41	91.18	86.66
Total				3232	91,137			
5 (400×)	87.60	96.66	90.62	558	6942	67.48	82.35	72.43
6 (400×)	89.97	80.68	86.87	640	6860	66.48	90.02	74.32
7 (400×)	98.50	96.25	97.75	252	7248	93.53	87.46	91.51
8 (400×)	82.39	91.98	85.58	300	5888	87.29	85.39	86.66
Total				1750	28,688			
9 (800×)	97.46	87.34	94.08	112	2960	87.30	90.40	88.33
10 (800×)	96.48	93.28	95.41	126	2646	73.58	85.23	77.46
11 (800×)	91.41	96.21	93.01	56	3016	97.19	60.22	84.86
12 (800×)	98.17	73.83	90.06	110	2962	90.12	61.11	80.45
13 (800×)	96.13	74.14	88.80	154	2918	75.93	87.11	79.66
Total				558	14,802			

The experiments were run with three different SVMs, trained respectively with 200×, 400× and 800× samples (the number of training instances extracted from each dataset and the total number of training instances are reported). Training instances are not included in the validation dataset.

partly intrinsic to tissue images (tissue's morphology is determined by a large number of unpredictable physiologic and pathologic parameters) and partly due to the preparation of the IHC samples, that is notoriously affected by many sources of variability (see Section 2). The variability of the features that are representative of the two tissues prevented the SVMs to develop a generalized model able to separate the two classes. This problem is obviously not limited to SVMs, that have often been shown to achieve better classification results compared to other learning methods across most applications [49], but it is rather related to any supervised approach (e.g. supervised ANN).

To the contrary, the performance of our unsupervised method is not compromised by features' variability, since the classification is based on the different characteristics of the two tissues in the current image, rather than on a fixed model of the ground truth.

In conclusion, our unsupervised technique was shown to provide selection of the target cancerous tissue highly comparable to manual approach and to overcome the limitations of supervised SVM techniques.

5.2. Segmentation of nuclei

Since the nuclear segmentation task is conceptually independent from the selection of the target tissue and the two procedures can be used separately, the experimental datasets used in this section were extracted from real-life tissue images only in the representative cancerous tumor areas; hence we validated nuclear segmentation independently from tissue selection. The experimental datasets were taken from both tissue samples with positive reactions to the EGF-R (membrane

activity) and to the TGF-alpha (cytoplasm activity) receptors; each dataset contained up to 137 cells, for a total number of 712 nuclei.

As for tissue selection task, the accuracy of nuclear segmentation was assessed through comparison with manual segmentations as well as through comparison with an alternate approach, namely active contours. The two validations are discussed in the following subsections.

5.2.1. Comparison with manual performance
We performed a two-levels evaluation of the performance of nuclear segmentation.

At a first level, we measured the skill of our automated procedure in identifying properly the cancerous nuclei, avoiding misdetections (e.g. of lymphocytes, neutrophils and sub-particles) and gross shape discrepancies as wrongly split or merged particles. A skilled operator was asked to evaluate the nuclear segmentations provided by our method, deriving from each dataset: (i) the number of acceptable detections, which may be used without errors in applications aimed at the automated measure of protein activity; (ii) the number of not detected nuclei, due to the local hard noise conditions or to stains superposition which may have covered the blue component up; (iii) the number of wrong detections, i.e. misdetection of foreign particles (e.g. of lymphocytes, neutrophils and sub-particles), particles splitting due to extreme intensity variations or merging of close couples of nuclei.

The achieved results are shown in Fig 6.

According to the evaluation provided by the expert of the field, our technique was successful for 83% of the particles; not detected particles were only 10% and errors were limited to 7% of the detections.

Tumor location	Type of staining	Nuclei correctly detected	Nuclei not detected	Wrong detections	Segmentation accuracy
Kidney	Cytoplasm	100%	0%	5.88%	91.77%
Liver	Cytoplasm	96.55%	3.45%	6.90%	89.07%
Prostate	Membrane	89.66%	6.90%	0%	84.76%
Bone marrow	Cytoplasm	93.94%	6.06%	9.09%	88.64%

Table 3 – Nuclear segmentation in tumor images from different anatomical locations.
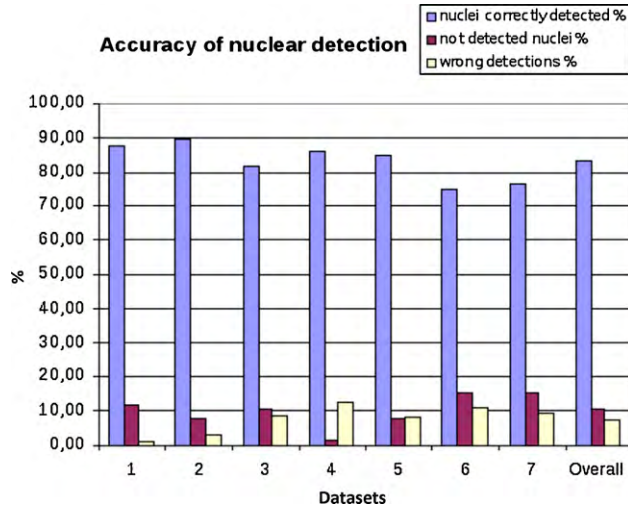
Fig. 6 – Accuracy of nuclear detection: in blue, percentage of nuclei correctly detected; in red, percentage of nuclei not detected; in yellow, percentage of wrong detections (i.e. misdetection of foreign particles, split nuclei, merged couples, etc.). (For interpretation of the references to color in this figure legend, the reader is referred to the web version of the article.)

The second level of the validation procedure consisted in the evaluation of the quality of the nuclear boundaries provided by our automated technique. This was achieved through a very strict pixel-wise comparison of the nuclear boundaries provided by the automated method with reference nuclei provided by manual operators. For each segmented nucleus, segmentation accuracy was estimated as:

$$\text{accuracy } (\%) = 100 \cdot \left[1 - \frac{\sum (R \oplus A)}{\sum (R + A)} \right], \tag{4}$$

where R is a binary image where pixels belonging to the reference manual nucleus are set to 1 and A is a binary image where pixels enclosed by the nuclear boundary provided by the automated procedure are set to 1. As shown by Fig. 7, $R \oplus A$ (logical XOR) returns the pixels that were misclassified

by the automated method (i.e. non-nuclear pixels classified as nuclear and vice versa), whereas $R + A$ (logical OR) returns the totality of the evaluated pixels: therefore accuracy is the complementary of the percentage of misclassification.

Manual segmentation of nuclei may lack reproducibility [29]: to improve the objectivity of our validation ten skilled operators were asked to outline manually the nuclear membrane of each tested nucleus. Thereafter, the reference nucleus used for the validation was generated by only those pixels that were enclosed by the most part of the ten manual boundaries.

The accuracy of nuclear segmentation achieved by our technique was on average 80.4%. This value was obtained by averaging the accuracy achieved in all the tested nuclei. The achieved results confirmed that our fully automated procedure provides nuclear segmentations that are comparable to manual segmentations (see Fig. 7 for an example of nucleus segmented with 80% accuracy).

In order to assess the robustness of our technique, we run experiments also in images of tumors from anatomical locations different from lung (kidney, liver, prostate and bone marrow, respectively). We tested our technique on validation datasets equivalent to the ones extracted from lung tissue and then we applied the same two-levels validation procedure applied to lung images. Therefore for each tissue type a pathologist quantified respectively the percentage of nuclei correctly detected, the percentage of nuclei not detected and the percentage of wrong detections. Then we quantified the nuclear segmentation accuracy compared to ten manual segmentations as in equation 4. The obtained results are reported in Table 3 and show accuracy values comparable with the lung tissue images.

5.2.2. Comparison with active contours approach

The performance of our technique was assessed also through extensive comparisons with a well known semi-automated technique, namely active contours.

Active contours (also called snakes) are a highly popular approach in computer vision and medical image segmentation. They are computer-generated curves that evolve iteratively within the image from an initial position toward the boundary of the target object (i.e. the nuclear membrane, in
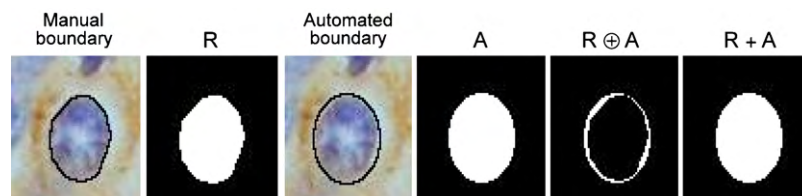
Fig. 7 – Calculation of segmentation's accuracy as in Eq. (4).

our application) through the minimization of an energy functional, that is generally a combination of an image term based on the characteristics of the image, an internal term based on the characteristics of the curve (e.g. tension and rigidity) and a user-defined constraint term (e.g. external forces).

Active contours are classified on the base of the image term guiding the evolving curve towards the target boundary as either: (i) edge-based snakes, with image energy based on gradient information; or (ii) region-based snakes, with image energy based on global image information (i.e. statistical features of the image). The former are usually more precise, since the image energy has sharp maxima at the gradient boundary; the latter are however less sensitive to curve initialization and to noise and they have less difficulties moving into deep concavities.

In this work we compared the performance of a semi-automated active contours procedure for nuclear segmentation in IHC tissue with the performance achieved by our morphology-based fully automated technique. The active contours procedure is based on the parametric spline-based active contour presented by [22], that is one of the most valuable in literature. Its main prerogatives are the cubic B-splines representation, which leads to the implicit smoothness of the curve thanks to the minimum curvature interpolation property, and the formulation of the image energy as linear combination of either edge-based (taking into account gradient magnitude as well as its direction) and region-based terms, thus inheriting the advantages of both. The simple modulation of the two terms leads to obtain a general unifying framework which includes all the most widely used formulations of active contours.

The active contours procedure for nuclear segmentation consists in feeding the above mentioned B-spline active contours with initial boundaries manually traced by an expert of the field; the information needed for the calculation of the image term is provided by the monochromatic blue image of hematoxylin stain, that identifies the nuclei. This monochromatic image is obtained through the already mentioned automated colors separation (see Section 3.2.1). The active contours automatically converge from the initial manual boundaries to the final boundaries through the minimization of their energy functional.

In order to perform an exhaustive comparison, we run experiments with three different formulations of active contours, respectively edge-based, region-based and mixed (i.e. with equally weighted linear combination of edge and region terms); as shown by Fig. 8, the active contours were initialized by the operator very close to the target boundaries, in order to obtain the higher performance achievable; in fact active contours are notoriously very sensitive to curve initialization.

The accuracy of nuclear segmentation was evaluated as reported in Eq. (4) through pixel-wise comparison with ten manual segmentations (see Section 5.2.1); then the results achieved by the three formulations of active contours were compared with the results achieved in the same validation dataset by our morphology-based technique. In particular, we evaluated: (i) the mean accuracy achieved by the different techniques, thus deducing which is statistically the best; (ii) the percentage of nuclei in which the best techniques exploited better accuracy than the other techniques: this adds meaningfulness to the previous result, since mean accuracy may be biased by few non-representative critical instances.

Our morphology-based technique obtained the best results: in fact its accuracy was on average higher than edge-based, mixed and region-based active contours' accuracy respectively of 8.2%, 10% and 11.8%. The achieved results, grouped according as the protein activity was localized in the cellular membrane (EGF-R receptor) or in the cytoplasm (TGF-alpha) of the validation samples, are shown in Fig. 9.

The superiority of the morphology-based approach was confirmed also by the second test, which established that our technique was more accurate than active contours in the most part of the tested nuclei. In particular our technique was more accurate than edge-based, mixed and region-based active contours respectively in 64%, 66% and 66% of the nuclei.

In conclusion, the morphology-based technique provides more accurate nuclear segmentations compared to active contours approach, despite they are manually initialized very close to the target membranes. The achieved results show that active contours are not expressive enough to handle complex and heterogeneous chromatic information in IHC: in fact they fail in detecting the nuclear region in presence of intensity gradients inside the region, as well as in presence of clustered particles (see Fig. 8).

A correct segmentation of nuclei in IHC tissue images requires high-level interpretation of the biological information carried by the color, which is actually not provided by any available active contours implementation.

5.3. Selection of cancerous tissue and segmentation of nuclei

In order to evaluate the combined accuracy of our proposed techniques as inserted in a pipeline for automated IHC analy-

Fig. 8 – Example of segmentation performed by active contours (initial manual boundary in blue, final boundary in red). (For interpretation of the references to color in this figure legend, the reader is referred to the web version of the article.)
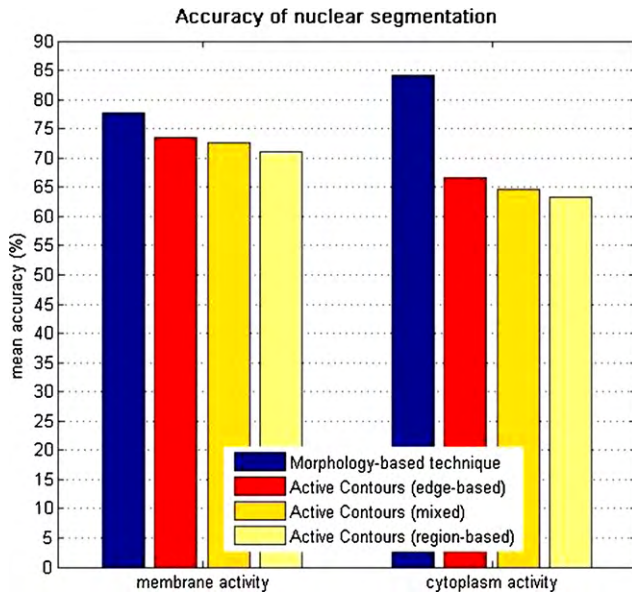
Fig. 9 – Mean percentage accuracy of nuclear segmentation achieved by respectively morphology-based approach, edge-based, mixed and region-based active contours in validation samples with membrane (EGF-R receptor) or cytoplasm (TGF-alpha receptor) activity.

sis, in this Section we provide a measure of how the efficiency of the tissue selection technique impacts on the following segmentation of pathological nuclei. This measure was obtained on the same dataset of real IHC images used in Section 5.1, where each sample included both pathological and non-pathological tissue. The experimental procedure for each of the validation images is the following: (i) we applied nuclear segmentation preceded by automated selection of the patho-

logical tissue; (ii) we applied nuclear segmentation preceded by manual selection of the pathological tissue as provided by a pathologist; (iii) we had the results obtained at points (i) and (ii) evaluated by a pathologist, in order to quantify the number of misdetected nuclei due to imprecise tissue selection. In particular the pathologist provided: (i) the number of nuclei that were missed by the nuclear segmentation technique due to pathological tissue classified as non-pathological and (ii) the number of nuclei that were incorrectly added to the segmentation results due to non-pathological tissue classified as pathological. The obtained results are shown in Table 4.

Summarizing, in our experiments nuclei missed or added incorrectly due to imprecise tissue selection were respectively 5.94% and 1.27% in the overall dataset consisting of a total number of 9216 cells, which confirms the efficiency of our proposed pipeline.

6. Conclusions

In this paper we presented an automated method for immuno-histochemical tissue image segmentation able to recognize cancerous areas disregarding non-pathological connective tissue and to perform accurate and precise segmentation of nuclear membranes within pathological areas. These two tasks are critical in order to obtain a reliable and standardized measure of the activity of specific proteins involved in the genesis and development of multi-factorial genetic pathologies. Moreover, the segmentations provided by our method can be exploited for any applications that require tissues and cells exploration.

We detailed all the steps of our proposed procedure and we demonstrated the high accuracy achievable thanks to our approach on a large dataset of real-life tissue images. Our method was able to perform cancer tissue selection with a 91% accuracy and to detect cancerous nuclei with a 83% accuracy;

Table 4 – Experimental results of the pipeline including both tissue selection and nuclear segmentation techniques.			
Dataset	Total number of nuclei	Missed nuclei (%)	Added nuclei (%)
1 (200×)	1537	6.31	2.47
2 (200×)	1411	7.44	1.2
3 (200×)	1498	0.67	0.47
4 (200×)	1225	3.18	1.47
Total (200×)	5671	4.43	1.41
5 (400×)	391	3.32	2.3
6 (400×)	500	12.2	0
7 (400×)	516	2.13	0
8 (400×)	322	12.11	0.62
Total (400×)	1729	7.17	0.64
9 (800×)	511	8.61	0
10 (800×)	419	8.11	0
11(800×)	261	1.53	8.43
12 (800×)	432	14.58	0
13 (800×)	193	13.99	2.07
Total (800×)	1816	9.47	1.43
Overall	9216	5.94	1.27

the pixel-wise comparison between the nuclear membranes provided by the algorithm and manually traced membranes returned a 95.2% accuracy value.

We compared our fully automated techniques with popular approaches in medical imaging and computer vision, namely support vector machines (SVMs) and active contours. Summarizing, our findings are the following: (i) our unsupervised morphology and color-based technique provides more accurate selection of cancerous tissue in IHC images compared to supervised SVM approach, whose performance is biased by the heterogeneity of the tissue features; (ii) our morphology and color-based technique provides better nuclear segmentations compared to semiautomated active contours, that are deviated from the target boundaries by noise or by overlapped and close particles; (iii) our morphology and color-based techniques provide tissue and nuclear segmentations that are highly comparable to manual segmentations; nevertheless, since our techniques are fully automated, they provide standardized and repeatable results.

In conclusion, our results demonstrated that our automated approach is effective and powerful, since it is able to overcome the limitations of the traditional segmentation methods as well as the slowness and the lack of repeatability of manual approach.

Acknowledgements

REFERENCES

[1] T.K. Taneja, S.K. Sharma, Markers of small cell lung cancer, World J. Surg. Oncol. 2 (10) (2004).

[2] M.J. Borad, R. Penny, M. Bittner, J. Gardner, S. Shack, E. Campbell, D. Taverna, R. Love, J. Trent, D. Von Hoff, Molecular profiling using immunohistochemistry (IHC) and DNA microarray (DMA) as a tool to determine potential therapeutic targets in patients who have progressed on multiple prior therapies, in: 1st AACR International Conference on Molecular Diagnostics in Cancer Therapeutic Development, 2006.

[3] E. Ficarra, G. De Micheli, S. Yoon, L. Benini, E. Macii, Joint co-clustering: co-clustering of genomic and clinical bioimaging data, Comput. Math. Appl. 55 (5) (2008) 938–949.

[4] Z. Theodosiou, I.N. Kasampalidis, G. Livanos, M. Zervakis, I. Pitas, K. Lyroudia, Automated analysis of FISH and immunohistochemistry images: a review, Cytometry A 71 (2007) 439–450.

[5] M. Lacroix-Triki, S. Mathoulin-Pelissier, J. Ghnassia, G. Macgrogan, A. Vincent-Salomon, V. Brouste, M. Mathieu, P. Roger, F. Bibeau, J. Jacquemier, High inter-observer agreement in immunohistochemical evaluation of HER-2/neu expression in breast cancer: a multicentre GEFPICS study, EJC 42 (17) (2006) 2946–2953.

[6] M. Cregger, A.J. Berger, D.L. Rimm, Immunohistochemistry and quantitative analysis of protein expression, Arch. Pathol. Lab. Med. 130 (7) (2006) 1026–1030.

[7] E.M. Brey, Z. Lalani, C. Johnston, M. Wong, L.V. McIntire, P.J. Duke, C.W. Patrick Jr., Automated selection of DAB-labeled tissue for immunohistochemical quantification, J. Histochem. Cytochem. 51 (5) (2003) 575–584.

[8] A.C. Ruifrok, R.L. Katz, D.A. Johnston, Comparison of quantification of histochemical staining by Hue-Saturation-Intensity (HSI) transformation and color deconvolution, Appl. Immunohistochem. 11 (1) (2004) 85–91.

[9] K.A. Divito, R.L. Camp, Tissue microarrays-automated analysis and future directions, Breast Cancer Online 8 (7) (2005).

[10] J. Cheng, J.C. Rajapakse, Segmentation of clustered nuclei with shape markers and marking functions, IEEE Trans. Biomed. Eng. 56 (3) (2009) 741–748.

[11] BioImagene Innovative Digital Pathology, http://www.bioimagene.com.

[12] H.D. Cualing, E. Zhong, L. Moscinski, Virtual flow cytometry of immunostained lymphocytes on microscopic tissue slides: iHCFlow™ tissue cytometry, Cytometry B 72 (2007) 63–76.

[13] Tissueqnostics Image Analysis System, http://www.tissuegnostics.com.

[14] Q. Huang, C. Yu, M. Klein, J. Fang, R.K. Goyal, DNA index determination with automated cellular imaging system (ACIS) in Barrett's esophagus: comparison with CAS 200, BMC Clin. Pathol. 5 (2005).

[15] Cambridge Research Inc., http://www.cri-inc.com.

[16] Aperio Scanscope, http://www.aperio.com.

[17] AQUA Automated Quantitative Analysis, http://www.historx.com.

[18] Y.J. Kim, B.F. Romeike, J. Uszkoreit, W. Feiden, Automated nuclear segmentation in the determination of the Ki-67 labeling index in meningiomas, Clin. Neuropathol. 25 (2) (2006) 67–73.

[19] F. Long, H. Peng, E. Myers, Automatic segmentation of nuclei in 3D microscopy images of *C. elegans*, in: ISBI, 2007, pp. 536–539.

[20] L. Yang, P. Meer, D.J. Foran, Unsupervised segmentation based on robust estimation and color active contour models, IEEE Trans. Inform. Technol. B 9 (3) (2005) 475–486.

[21] D.P. Mukherjee, N. Ray, S.T. Acton, Level set analysis for leukocyte detection and tracking, IEEE Trans. Image Process 13 (4) (2004) 562–572.

[22] M. Jacob, T. Blu, M. Unser, Efficient energies and algorithms for parametric snakes, IEEE Trans. Image Process 13 (9) (2004) 1231–1244.

[23] B. Zhang, C. Zimmer, J.C. Olivo-Marin, Tracking fluorescent cells with coupled geometric active contours, in: ISBI, 2004, pp. 476–479.

[24] J. Cheng, J.C. Rajapakse, Segmentation of clustered nuclei with shape markers and marking function, IEEE Trans. Biomed. Eng. 56 (2009) 741–748.

[25] G. Landini, I.E. Othman, Estimation of tissue layer by sequential morphological reconstruction, J. Microsc. 209 (2) (2003) 118–125.

[26] A. Pinidiyaarachchi, C. Wahlby, Seeded watersheds for combined segmentation and tracking of cells, in: ICIAP05, vol. 3617, 2005, pp. 336–343.

[27] P.R. Gudla, K. Nandy, J. Collins, K.J. Meaburn, T. Misteli, S.J. Lockett, A high-throughput system for segmenting nuclei using multiscale techniques, Cytometry A 73 (2008) 451–466.

[28] H. Masmoudi, S.M. Hewitt, N. Petrick, K.J. Myers, M.A. Gavrielides, Automated quantitative assessment of HER-2/neu immunohistochemical expression in breast cancer, IEEE Trans. Med. Imaging 28 (2009) 916–925.

[29] S. Naik, S. Doyle, S. Agner, A. Madabhushi, M. Feldman, J. Tomaszewski, Automated gland and nuclei segmentation for grading of prostate and breast cancer histopathology, in: ISBI, 2008, pp. 284–287.

[30] Y. Boykov, G. Funka-Lea, Graph cuts and efficient N-D images segmentation, Int. J. Comput. Vis. 70 (2) (2006) 109–131.

[31] B.L. Luck, K.D. Carlson, A.C. Bovik, R.R. Richards-Kortum, An image model and segmentation algorithm for reflectance confocal images of in vivo cervical tissue, IEEE Trans. Image Process 14 (9) (2005) 1265–1276.

[32] A.C. Wolff, M.E. Hammond, J.N. Schwartz, K.L. Hagerty, D.C. Allred, R.J. Cote, M. Dowsett, P.L. Fitzgibbons, W.M. Hanna, A. Langer, L.M. McShane, S. Paik, M.D. Pegram, E.A. Perez, M.F. Press, A. Rhodes, C. Sturgeon, S.E. Taube, R. Tubbs, G.H. Vance, M. van de Vijver, T.M. Wheeler, D. Hayes, American Society of Clinical Oncology/College of American Pathologists guideline recommendations for human epidermal growth factor receptor 2 testing in breast cancer, Arch. Pathol. Lab. Med. 131 (2007).

[33] E. Ficarra, E. Macii, Computer-aided evaluation of protein expression in pathological tissue images, in: CBMS06, 2006, pp. 413–418.

[34] C. Lopez, M. Lejeune, M.T. Salvado, P. Escriva, R. Bosch, L.E. Pons, T. Alvaro, J. Roig, X. Cugat, J. Baucells, J. Jaen, Automated quantification of nuclear immunohistochemical markers with different complexity, Histochem. Cell Biol. 129 (2008) 379–387.

[35] S.P. Zehntner, M.M. Chakravarty, J.R. Bolovan, C. Chan, B.J. Bedell, Synergistic tissue counterstaining and image segmentation techniques for accurate, quantitative immunohistochemistry, J. Histochem. Cytochem. 56 (10) (2008) 873–880.

[36] T.J. Fuchs, T. Lange, P. Wild, H. Moch, J. Buhmann, Weakly supervised cell nuclei detection and segmentation on tissue microarrays of renal clear cell carcinoma, in: DAGM08, vol. 5096, 2008, pp. 173–182.

[37] L. Wang, Support vector machines: theory and applications, Stud. Fuzziness Soft Comput. 177 (2005).

[38] P. Matula, A. Kumar, I. Worz, H. Erfle, R. Bartenschlager, R. Eils, K. Rohr, Single-cell-based image analysis of high-throughput cell array screens for quantification of viral infection, Cytometry A 75 (4) (2009) 309–318.

[39] T. Markiewicz, P. Wisniewski, S. Osowski, J. Patera, W. Kozlowski, R. Koktysz, Comparative analysis of methods for accurate recognition of cells through nuclei staining of Ki-67 in neuroblastoma and estrogen/progesterone status staining in breast cancer, Anal. Quant. Cytol. Histol. 31 (1) (2009) 49–62.

[40] A.C. Ruifrok, D.A. Johnston, Quantification of histochemical staining by color deconvolution, Anal. Quant. Cytol. Histol. 23 (4) (2001) 291–299.

[41] G. Landini, Software, http://www.dentistry.bham.ac.uk/landinig/software/software.html.

[42] S. Di Cataldo, E. Ficarra, E. Macii, Automated discrimination of pathological regions in tissue images: unsupervised clustering vs supervised SVM classification, Commun. Comput. Inform. Sci. (2008) 344–356.

[43] A.K. Jain, R.C. Dubes, Algorithms for Clustering Data, Prentice Hall, 1988.

[44] R.C. Gonzalez, R.E. Woods, Digital Image Processing, 3rd ed., Prentice Hall, Upper Saddle River, NJ, 2007.

[45] W.S. Rasband, ImageJ, U.S. National Institutes of Health, Bethesda, Maryland, USA, http://rsb.info.nih.gov/ij/.

[46] R. Couture, Local Thresholding and Unsharp Masking by Median Filtering, http://www.aecom.yu.edu/aif/instructions/imagej/macros/local-threshold-unsharp-masking.txt.

[47] J. Sacha, K-means Clustering, http://ij-plugins.sourceforge.net/plugins/clustering/index.html.

[48] T. Twellmann, T.W. Nattkemper, W. Schubert, H. Ritter, Cell detection in micrographs of tissue sections using support vector machines, in: ICANN2001, 2001, pp. 79–88.

[49] A. Statnikov, C.F. Aliferis, I. Tsamardinos, D. Hardin, S. Levy, A comprehensive evaluation of multicategory classification methods for microarray gene expression cancer diagnosis, Bioinformatics 21 (5) (2005) 631–643.